Si-CMOS Compatible Synthesis of Wafer-Scale 1T-CrTe$_2$ with Step-Like Magnetic Transition

Jiwei Liu, Cong Wang, Yuwei Wang, Jianbin Xu, Wei Ji,* Mingsheng Xu,* and Deren Yang*

2D room-temperature ferromagnet CrTe$_2$ is a promising candidate material for spintronic applications. However, its large-scale and cost-effective synthesis remains a challenge. Here, the fine controllable synthesis of wafer-scale 1T-CrTe$_2$ films is reported on a SiO$_2$/Si substrate using plasma-enhanced chemical vapor deposition at temperatures below 400 °C. Magnetic hysteresis measurements reveal that the synthesized 1T-CrTe$_2$ films exhibit perpendicular magnetic anisotropy along with distinct step-like magnetic transitions. It is found that 1T-CrTe$_2$ is susceptible to oxygen adsorption even in ambient conditions. The theoretical calculations indicate that the oxidation of surface layers is crucial for the absence of out-of-plane easy axis in few-layer CrTe$_2$, while the interlayer antiferromagnetic coupling among the upper surface layers leads to the observed step-like magnetic transitions. The study provides a Si-CMOS compatible approach for the fabrication of magnetic 2D materials and highlights how unintentional adsorbents or dopants can significantly influence the magnetic behaviors of these materials.

J. Liu, D. Yang
State Key Laboratory of Silicon and Advanced Semiconductor Materials
School of Materials Science and Engineering
Zhejiang University
Hangzhou 310027, P. R. China
E-mail: mseyang@zju.edu.cn
J. Liu, C. Wang, W. Ji
Beijing Key Laboratory of Optoelectronic Functional Materials
& Micro-Nano Devices
Key Laboratory of Quantum State Construction and Manipulation
(Ministry of Education)
School of Physics
Renmin University of China
Beijing 100872, P. R. China
E-mail: wji@ruc.edu.cn
J. Liu, Y. Wang, M. Xu
College of Integrated Circuits
State Key Laboratory of Silicon and Advanced Semiconductor Materials
Zhejiang Key Laboratory of Advanced Micro-nano Transducers Technology
Zhejiang University
Hangzhou 310027, P. R. China
E-mail: msxu@zju.edu.cn
J. Xu
Department of Electronic Engineering and Materials
Science and Technology Research Centre
The Chinese University of Hong Kong
Shatin, New Territories, Hong Kong, SAR 999077, P. R. China

1. Introduction

The discovery of 2D intrinsic ferromagnets CrI$_3$,[1] and Cr$_2$Ge$_2$Te$_6$.[2] confirmed the existence of long-range ferromagnetic (FM) order in 2D systems, challenging the long-standing belief that such order cannot exist in isotropic 2D systems at finite temperatures.[3] Few-layer CrI$_3$ has perpendicular magnetic anisotropy (PMA) and its interlayer antiferromagnetically coupling leads to layer-dependent magnetism. Monolayer CrI$_3$ exhibits rectangular hysteresis in the Kerr rotation, a characteristic of Ising-like ferromagnetism, while bilayer CrI$_3$ of HT phase (C$_{2/m}$) shows a plateau in the magneto-optical Kerr effect (MOKE) signal at field values of ± 0.65 T due to the interlayer antiferromagnetic (AFM) coupling.[4,5] In comparison, Fe$_{3+x}$GeTe$_2$ (FGT) is another prototypical van der Waals (vdW) ferromagnet with a Curie temperature (T$_C$) ranging from 130 to 230 K,[6–8] which, while higher than that of CrI$_3$ (45–61 K),[1] still substantially below room temperature. The pursuit of high Curie temperature ferromagnets in 2D materials has garnered significant interest, yet only a few room temperature ferromagnetic materials, such as CrS$_2$,[9,10] CrSe,[11] CrTe$_2$,[12,13] Cr$_3$Te$_4$,[14] Cr$_{0.87}$Te,[15] Cu$_2$Cr$_2$Te$_4$,[16] Fe$_5$GeTe$_2$,[17] and Fe$_3$GaTe$_2$,[18] have been reported so far.

Bulk 1T-CrTe$_2$, a transition metal dichalcogenide (TMD) with a T$_C$ of ≈ 310 K,[19] appears to be a promising candidate material for room-temperature spintronic applications. However, it faces at least two significant challenges: the achievement of large-scale energy-efficient fabrication and the determination of magnetic properties. Specifically, 2D 1T-CrTe$_2$ single crystals ($\approx 60\,\mu$m in diameter) have been synthesized on SiO$_2$/Si substrates via chemical vapor deposition (CVD) at 710 °C using CrCl$_2$ and Te powders.[20] This high fabrication temperature significantly exceeds the compatibility limits of Si-COMS technologies. The molecular beam epitaxy (MBE) technique reduces the growth temperature to 375 °C for preparing Te-capped 1T-CrTe$_2$ layers on bilayer graphene formed on a SiC surface.[21] A more complex MBE process further lowers the growth temperature to 240–270 °C, however, it involves multiple process steps, including an initial epitaxial growth of a Bi layer followed by transformation to Bi$_2$Te$_3$ as a buffer layer for growth of granular 1T-CrTe$_2$ layers on SiN$_x$ substrates.[22] Thus, there is a pressing need for a growth method that can produce large-scale samples in a Si-CMOS compatible, energy-efficient, and straightforward manner for CrTe$_2$ production.

ADVANCED
SCIENCE NEWS

www.advancedsciencenews.com

ADVANCED
MATERIALS

www.advmat.de

Moreover, the magnetization properties have been debated among samples prepared using different methods. The CVD-prepared crystal exhibits a distinctive step-like feature in their magnetic hysteresis (M-H) loops.[20] While similar phenomena were observed on the granular 1T-CrTe$_2$ layers grown via MBE, no step-like feature was observed in the Te-capped MBE 1T-CrTe$_2$ layers. Additionally, the Te-capped MBE 1T-CrTe$_2$ samples (2–35 L) display an out-of-plane magnetic easy axis,[20–22] whereas density functional theory (DFT) calculations suggested that the easy axis of intrinsic few layer 1T-CrTe$_2$ should align in the in-plane direction.[23] Therefore, clarifying the physical origins of this discrepancy in magnetization direction and the step-like behavior observed in M-H loops is essential for advancing its potential applications.

In this study, we utilized plasma-enhanced chemical vapor deposition (PECVD) method to synthesize uniform wafer-scale 1T-CrTe$_2$ films on SiO$_2$ (300 nm)/Si substrates using pre-deposited Cr film and Te powder at temperatures below 400 °C. We also investigated their magnetization properties, revealing that our 1T-CrTe$_2$ films (6–18 L) exhibit an out-of-plane easy axis along with step-like magnetic transitions. Through DFT calculations, we found that the oxidation of 1T-CrTe$_2$ surface layers plays a critical role in determining the magnetic easy-axis orientation and attributed the observed step-like features in M-H loops to the absence of local interlayer antiferromagnetic (AFM) coupling in upper surface layers.

2. Results and Discussion

Our low-temperature synthesis of wafer-scale CrTe$_2$ on SiO$_2$ (300 nm)/Si is realized with the assistance of H$_2$/Ar plasma (**Figure 1a**). We first deposited a 1–3 nm thick layer of Cr on the substrate using magnetron sputtering as a seed layer. Considering the instability of H$_2$Te gas, we chose Te powders as tellurium precursors. Previously, Ahn et al. reported the formation of ionized H$_3$S$^+$ ions during their PECVD synthesis of MoS$_2$.[24] In the process of our PECVD, it is inferred that Te may react with ionized H$_2$/Ar plasma first to form H$_3$Te$^+$ ions as we can see the color of plasma changing from pink to bright white during the process. We further find that CrTe$_2$ cannot be synthesized below 400 °C if no H$_2$/Ar plasma is involved. Thus, the generated H$_3$Te$^+$ ions activate Cr atoms and react with them to form CrTe$_2$. The detailed Experimental Section are shown in Experimental Section and Figure S1 (Supporting Information). By this method, smooth and uniform wafer-scale CrTe$_2$ films (Figure 1c) can be easily produced. As revealed by the atomic force microscopy measurement, when the thickness of the Cr seed layer is 1, 2, and 3 nm, the thickness of as-grown CrTe$_2$ is ≈3.8, 7.3, and 11 nm, respectively (Figure S2, Supporting Information). This relationship of thickness between the Cr seed layer and 1T-CrTe$_2$ film can be deduced from the atomic radius of the Cr atom. It is assumed that all Cr atoms of a 1 nm film stack in *bcc* structure, the lattice constant *a* can be calculated by the equation: $a = \frac{4r_{Cr}}{\sqrt{3}}$. The atomic radius of Cr in crystals is 140 pm,[25] hence the lattice constant *a* is 323.3 pm. In other words, there should be 7 layers of Cr in a 1 nm film that transformed into 7L 1T-CrTe$_2$. However, since the deposited Cr films are generally amorphous and the atomic stacking is much less compact than the *bcc* stacking, the actual

1T-CrTe$_2$ film we obtained is thinner than the theoretical value. In our work, ≈6L of 1T-CrTe$_2$ can be obtained from 1 nm Cr film.

We characterize the atomic arrangement structures of the synthesized CrTe$_2$ films. The Raman spectra (Figure 1d) collected at 16 different points across the 2-inch CrTe$_2$ thin film displays two prominent peaks, i.e., 121.5 cm^{-1} for E$_{2g}$ vibration mode and 141.3 cm^{-1} for A$_{1g}$ vibration mode. The Raman peaks of CVD-grown 1T-CrTe$_2$ flakes were reported at 123 cm^{-1} (E$_{2g}$) and 143 cm^{-1} (A$_{1g}$).[20] In the case of exfoliated 1T-CrTe$_2$ flakes without h-BN encapsulation, the Raman peaks were at 125.5 cm^{-1} (E$_{2g}$) and 145 cm^{-1} (A$_{1g}$).[13] Further, the two Raman peaks of freshly exfoliated or sealed flakes were observed at 102 cm^{-1} (E$_{2g}$) and 134 cm^{-1} (A$_{1g}$), which were shifted to 126 cm^{-1} (E$_{2g}$) and 142 cm^{-1} (A$_{1g}$) after one week of exposure to air.[26] Therefore, the Raman features of our sample confirm the formation of uniform 1T phase of the as-grown CrTe$_2$ films, and the samples may be partially oxidized due to exposure to the ambient environment. The XRD patterns for our PECVD-synthesized 1T-CrTe$_2$ film (Figure S3, Supporting Information) with peaks at $2\theta = 29.8°$ correspond to the (0 0 2) diffraction. The *d* spacing is 5.996 Å as calculated based on the Bragg equation, which agrees with the previous reports.[20,27] For the wafer-scale 1T-CrTe$_2$ film, we also capture streaky reflection high-energy electron diffraction (RHEED) patterns (Figure S11, Supporting Information) from any direction, which indicates the polycrystalline structure of our sample. Auger Electron Spectroscopy (AES) technique is a powerful technique for 2D materials study,[28,29] which can determine the composition and distribution of elements in atomic-thick 2D materials. The AES element analysis of our 1T-CrTe$_2$ sample (Figure 1e) gives the Te: Cr concentration ratio of ≈2:1. We also detect an O signal by the AES, which is due to the adsorption of oxygen atoms on the surface and the oxidation of the 1T-CrTe$_2$ surface when the sample was exposed to the air as addressed below. An aberration-corrected scanning transmission electron microscope (ac-STEM) was further used to characterize the atomic structure of the CrTe$_2$ films as shown in Figure 1f,g. Since the Te atom has a higher atomic number than the Cr atom, Te atoms have a brighter contrast in the images. The atomic resolution STEM-HAADF image shows each Cr atom is surrounded with six Te atoms arranged into a hexagonal lattice with the lattice parameters of a = b = 3.80 Å, consistent with the atomic configuration of 1T phase.[23] The cross-sectional image of 1T-CrTe$_2$ substantiates a regular layered structure (Figure 1h), and the energy-dispersive X-ray spectroscopy (EDX) (Figure S4, Supporting Information) indicates the homogeneous distribution of Cr atoms and Te atoms with Te/Cr ratio of ≈2:1.

We investigate the plasma power and temperature effects on the synthesis of 1T-CrTe$_2$ films to achieve precise control over the synthesis process. First, CrTe$_2$ films were synthesized at the same temperature but with different plasma powers of 50, 150, and 300 W and analyzed by the AES Profile technique (see Experimental Section for more details). The distribution of samples' atomic concentrations as a function of depth can be obtained using the AES Profile technique. Disregarding electron beam irradiation damage, the relative ratio of Te atoms to Cr atoms should be 2 in any detective depth theoretically. **Figure 2a** shows the ratio of Te/Cr at different depths of the samples, which can reflect the reaction degree between the Te and Cr atoms. It is found that Te atoms could react with Cr atoms as long as the plasma power
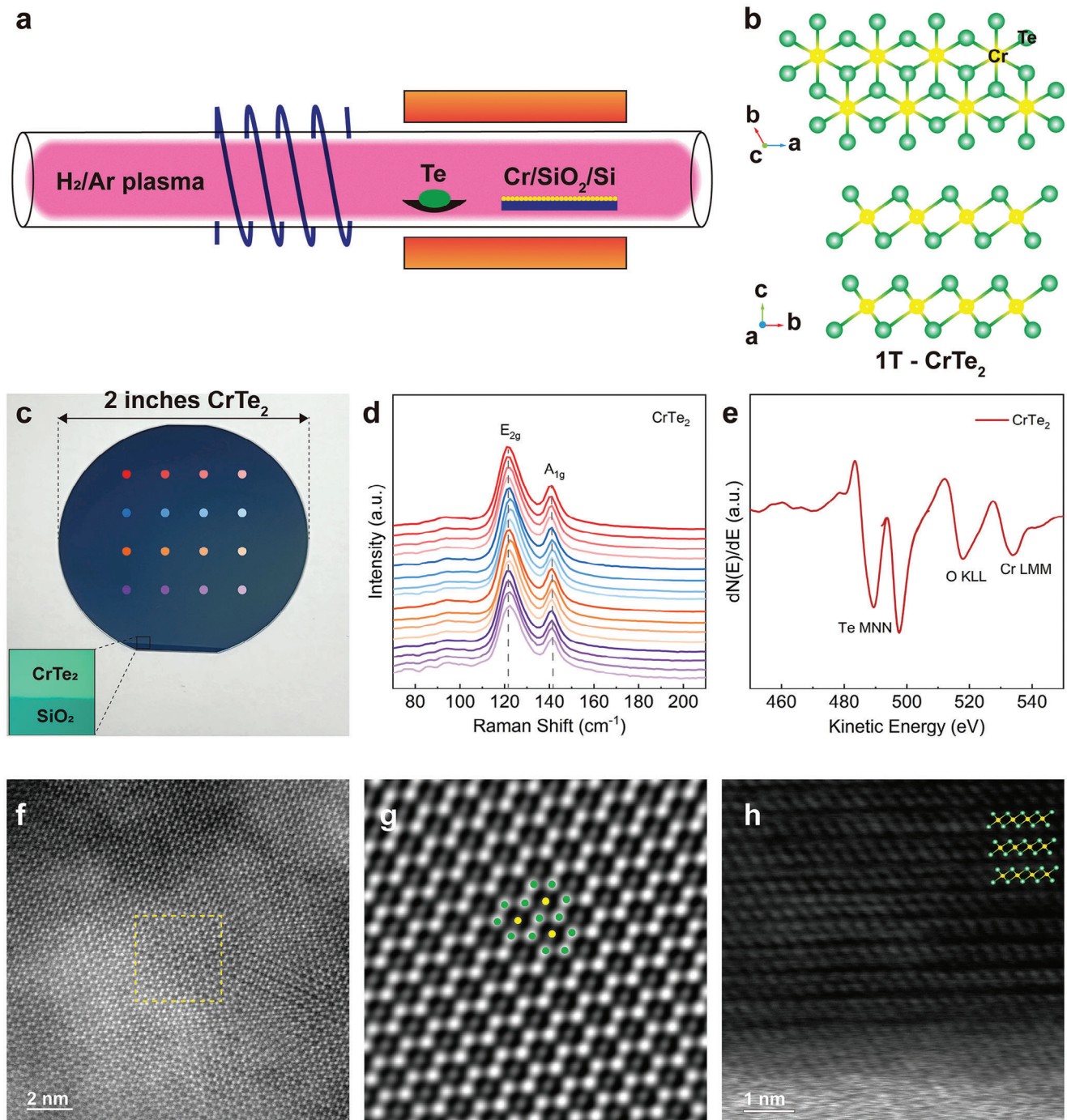
ADVANCED
SCIENCE NEWS

www.advancedsciencenews.com

**ADVANCED
MATERIALS**

www.advmat.de

Figure 1. Wafer-scale synthesis of 1T-CrTe$_2$ thin films by PECVD. a) Schematic illustration of the synthesis process of 1T-CrTe$_2$. b) Top and side views of the atom arrangement in 1T-CrTe$_2$ crystal structure. c) Photograph of wafer-scale 1T-CrTe$_2$ film synthesized on a 2-inch SiO$_2$/Si substrate. The inset is the optical microscope image of as-grown 1T-CrTe$_2$. d) Raman spectra of 16 different points on a 2-inch 1T-CrTe$_2$ sample. The 16 collected points with different colors are shown in (c). e) AES spectrum of the 1T-CrTe$_2$ sample. f) Atomic resolution STEM high-angle annular dark-field (HAADF) image, and g) the corresponding inverse FFT (IFFT) image. The green dots represent Te atoms, and the yellow dots represent Cr atoms. h) STEM image of the 1T-CrTe$_2$ viewed in cross-section.
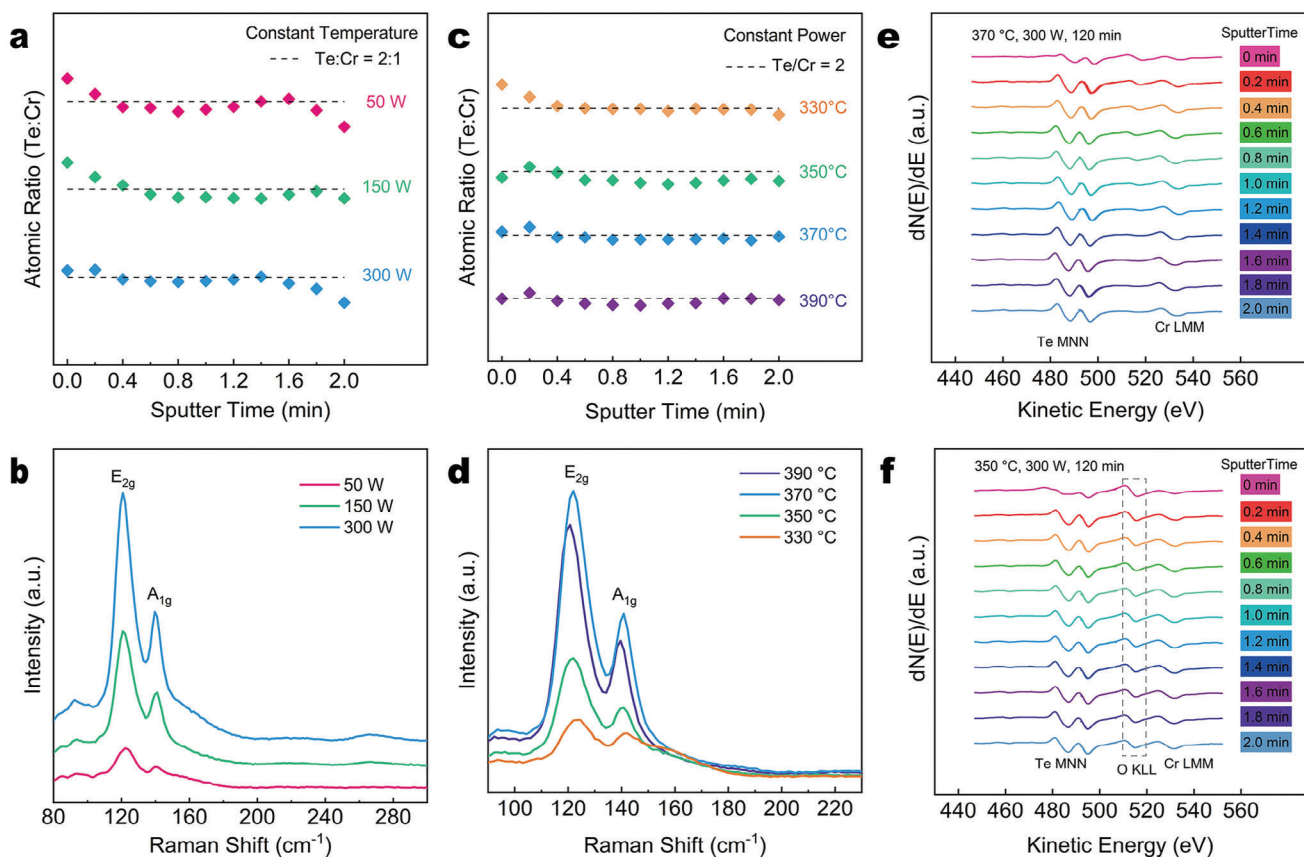
ADVANCED
SCIENCE NEWS
www.advancedsciencenews.com

**ADVANCED
MATERIALS**
www.advmat.de

Figure 2. 1T-CrTe$_2$ films synthesized at different conditions by PECVD. a) Te/Cr atomic ratio and b) Raman spectra of the corresponding 1T-CrTe$_2$ synthesized with different plasma powers at 370 °C. c) Te/Cr atomic ratio and d) Raman spectra of corresponding 1T-CrTe$_2$ synthesized at different temperatures with 300 W. e,f) AES spectra to varying depths of the 1T-CrTe$_2$ synthesized at (e) 370 °C, 300 W and f) 350 °C, 300 W.

was not zero, and the Te/Cr ratio is close to 1.9:1. When the accumulation of etching time reaches 2 min, the ratio of Te/Cr has a significant deviation from 2:1, because the sample was almost etched away, and the structure of CrTe$_2$ may be destroyed by the long-time exposure to Ar ion. The full width at half maximum (FWHM)[30,31] and intensity[32] of the Raman spectrum are indicators for crystalline quality; the smaller FWHM and higher intensity represent better crystalline quality. As shown in Figure 2b, we collect a series of Raman spectra in the same test conditions to reveal the relationship between crystalline quality and plasma power. The FWHM of each Raman spectrum in Figure 2b is calculated as 13.1 cm^{-1} for 50 W, 12.6 cm^{-1} for 150 W, and 11.7 cm^{-1} for 300 W, respectively. Moreover, the Raman intensity of each spectrum increases monotonously with the increase of plasma power. All these results indicate that H$_2$/Ar plasma could reduce the reaction barrier and promote the reaction of Cr and Te atoms to obtain a better crystalline quality. Second, we synthesized 1T-CrTe$_2$ films at different temperatures (330, 350, 370, and 390 °C) with the same plasma power of 300 W. As found in Figure 2c,d, the samples synthesized at 330 and 370 °C have a relatively consistent Te/Cr atomic ratio except the oxidized surface layers (corresponding to sputter time of 0–0.2 min), and the ratio is close to 2:1, while the atomic ratio of the samples synthesized at 350 °C and 390 °C is close to 1.8:1. It can be derived from the Raman spectra that the FWHMs are 14.1 cm^{-1} for 330 °C, 12.9 cm^{-1}

for 350 °C, 12.4 cm^{-1} for 370 °C, and 13.6 cm^{-1} for 390 °C, respectively, and the intensity of E$_{2g}$ or A$_{1g}$ increases first and then decreases with the increase of the synthesis temperature. Among them, the 1T-CrTe$_2$ samples synthesized at 370 °C have the smallest FWHM and highest intensity of the Raman spectrum, indicating the best crystalline quality. Although the Te/Cr atomic ratio of the samples synthesized at 330 °C is very close to 2:1, the large FWHM and weak Raman peak intensity indicate it is more likely to an amorphous structure rather than a highly crystalline structure. Moreover, we surprisingly find that the 1T- CrTe$_2$ film synthesized at 370 °C with 300 W has negligible oxygen content inside the sample as observed on the weak O KLL signal in the AES spectra (Figure 2e). In contrast, the O KLL signal is intensive in the 1T-CrTe$_2$ film synthesized at 350 °C and 300 W (Figure 2f). These results indicate higher synthesis temperature could facilitate the formation of 1T-CrTe$_2$ and exorcise oxygen in samples.

To study the role of the O atoms in the synthesis of CrTe$_2$, we deliberately terminate the reaction process and investigate the compositions of the sample. As observed on **Figure 3**, the etching of the sample by Ar ions for 0.4 min removed the O atoms on the surface (Figure 3a,d) but could not completely etch away the CrTe$_2$ (Figure 3b,c). Although further etching another 0.8 min removed the CrTe$_2$ layer (Figure 3c), strong Cr LMM and O KLL signals are observed (Figure 3b,d). This suggests the co-existence of O and Cr but without Te in the sample after etching for 1.2 min,
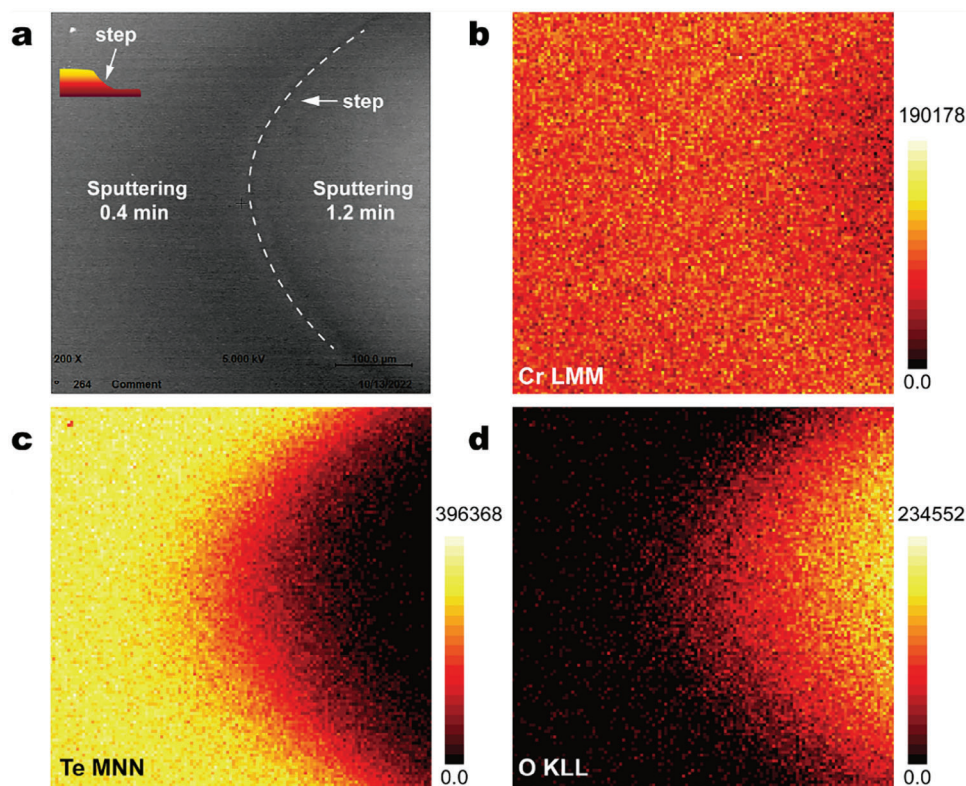
**ADVANCED
SCIENCE NEWS**

www.advancedsciencenews.com

**ADVANCED
MATERIALS**

www.advmat.de

Figure 3. Profile elemental distributions of incompletely reacted 1T-CrTe$_2$ sample. a) SEM image of the CrTe$_2$ surface and the step etched by Ar ions. b) Cr LMM Auger electron mapping. c) Te MNN Auger electron mapping. d) O KLL Auger electron mapping.

i.e., the oxidization of the Cr layer occurred prior to tellurization (Figure 3d). These results indicate that Te and O coexist to form CrO$_x$Te$_y$ at the initial stage of the reaction and as the reaction progresses, O atoms are gradually replaced by Te atoms, and finally, CrTe$_2$ is formed. In addition, we perform an AES depth profile of the Cr seed layer, and the results show that the O atoms do come from the oxidation of the Cr layer rather than the SiO$_2$/Si substrate (Figure S5, Supporting Information). Previously, Liang et al. used AES to study the intermediate process of MoS$_2$ grown by a CVD method.[33] Their results showed that O and S coexisted in the sample at the initial nucleation stage and the O signal disappeared when the reaction was over. Based on the above results and considering the Cr layer is easily oxidized as exposed to air, the seed layer for our synthesis could be CrO$_x$. Therefore, the mechanism for synthesizing 1T-CrTe$_2$ using PECVD is as follows: 1) H$_2$/Ar plasma controls the reaction by reducing reaction temperature. Without plasma assistance, Cr and Te do not react below 400 °C (Figure S6, Supporting Information). 2) The H$_2$/Ar plasma activates both the Te powder to first form H$_3$Te$^+$ and the CrO$_x$. 3) The CrO$_x$ seeding layer is first tellurized into the intermediate state of CrO$_x$Te$_y$ and finally becomes CrTe$_2$, accompanied by the generation of by-product H$_2$O.

We measure M-H loops of our as-synthesized 1T-CrTe$_2$ films using SQUID-VSM under magnetic fields parallel and vertical to the c-axis of the film. **Figure 4a,b** illustrate the M-H curves of ≈7 nm and ≈11 nm thick 1T-CrTe$_2$ films under 5, 100, 150, and 300 K, respectively. The two samples exhibit colossal out-of-plane magnetic moments but feeble in-plane moments. Moreover, the

room-temperature magnetic features are observed on both samples. Surprisingly, a striking step-like feature is presented in the M-H curves when the measured temperature is below 100 K. Previously, a similar but weak phenomenon in the CVD-grown 1T-CrTe$_2$ crystals was observed, which was attributed to a complex magnetic domain structure.[20] Such step-like features were also observed on some other systems with labyrinthine magnetic domains.[7,34–37] In our results (Figure 4a,b, dark blue and dark red M-H curves at 5 K), once the out-of-plane field switches from +0 T to −0.5 T, some moments sensitively start canting, which leads to a decrease in magnetization. In comparison, the remaining moments switch their directions until the field reaches ≈1.2 T, and vice versa. It's also noticed that when the magnetic field is vertical to the c-axis, the M-H curves are faint, and the values of M$_s$ are far less than those at the field parallel to the c-axis. We further fabricate Hall bar devices of the 1T-CrTe$_2$ film for electrical transport measurement at 10 K, 100 K, and room temperature (RT) to prove the perpendicular magnetic anisotropy (PMA). The square R$_{AHE}$ signal (shown in Figure S12b, Supporting Information) is clearly observed at 10 and 100 K, which strongly demonstrates the PMA. However, the RT R$_{AHE}$ signal is not as clear as those at lower temperatures. This phenomenon may be ascribed to the degradation of the 1T-CrTe$_2$ incurred by the Hall bar device fabrication process. Furthermore, the step-like magnetic transition is surface-sensitive. Besides the oxygen influence on the 1T-CrTe$_2$ top surface layers, the fabrication of the Au/Ti electrodes on the top surface of the CrTe$_2$ may damage the surface layers of 1T-CrTe$_2$. We will address the origins of such
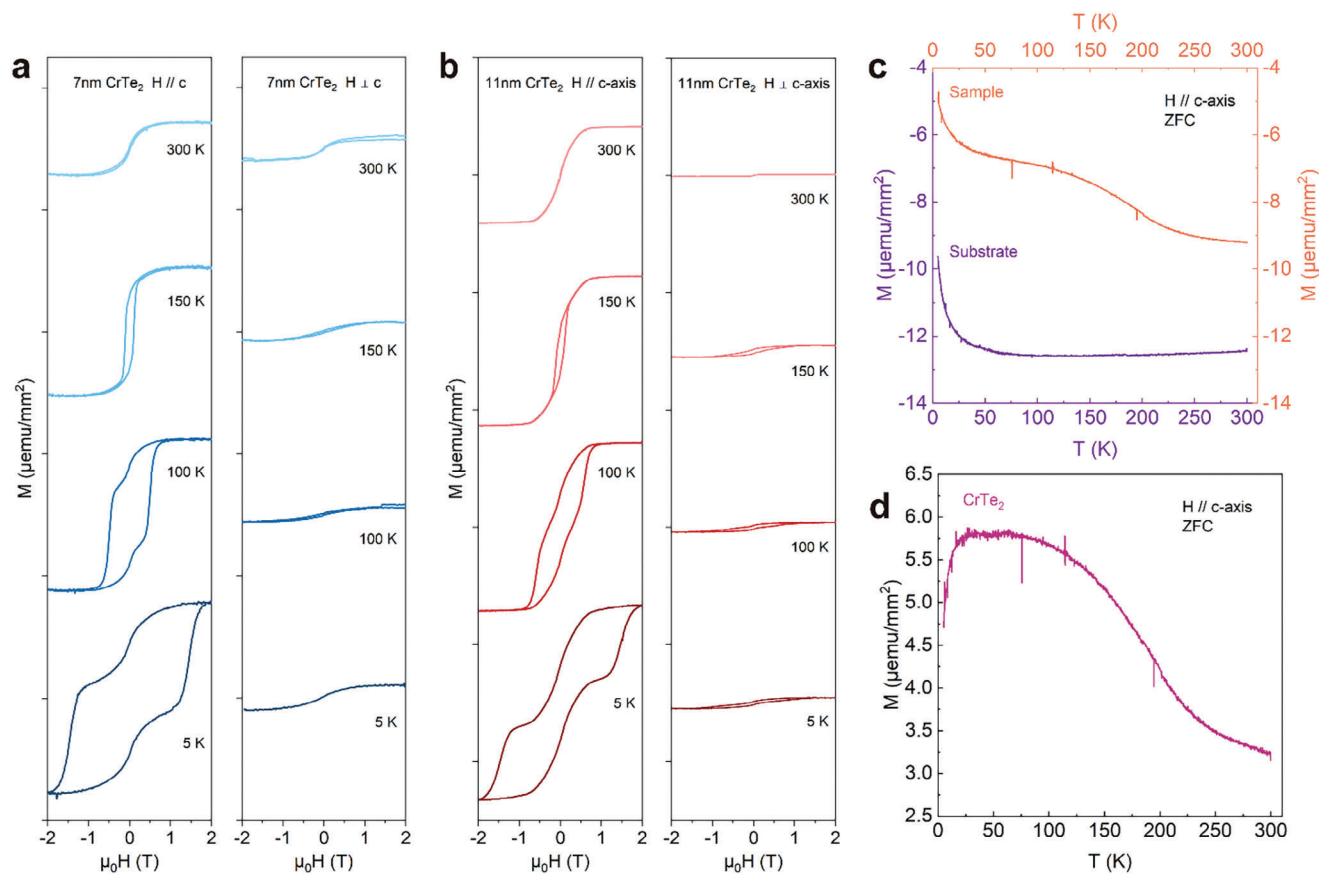
**ADVANCED
SCIENCE NEWS**

www.advancedsciencenews.com

**ADVANCED
MATERIALS**

www.advmat.de

Figure 4. Magnetic properties of 1T-CrTe$_2$ films grown by PECVD. a,b) Magnetic hysteresis loops for 1T-CrTe$_2$ films with thickness of ≈7 nm (a) and ≈11 nm (b) under the magnetic field parallel and vertical to the c-axis, respectively. c,d) M-T curves under an out-of-plane magnetic field of 2 T for (c) 1T-CrTe$_2$ /SiO$_2$/Si sample, SiO$_2$/Si substrate, and (d) 1T-CrTe$_2$ film.

observation by performing DFT calculations later. Figure 4c,d and Figure S13 (Supporting Information) display the magnetization versus temperature (M-T) curves under an out-of-plane magnetic field of 2 T for the 11 nm 1T-CrTe$_2$ film. The cooling process was conducted under zero field. Because the diamagnetic SiO$_2$ (300 nm)/Si (400 μm) substrate is much thicker than the CrTe$_2$ film, the signal of the CrTe$_2$/SiO$_2$/Si sample is diamagnetic (Figure 4c). We measured the M-T curve of a pure SiO$_2$/Si substrate (Figure 4c) to obtain the real magnetic signal of 1T-CrTe$_2$ (Figure 4d). It is found that the magnetization first increases and then decreases with the decrease in temperature, which is the character of antiferromagnetic orders. However, it is undeniable that the peak on the M-T curve is not sharp enough to define the Neel temperature, which indicates only part of the magnetic order exhibits antiferromagnetism.

We perform DFT calculations to elucidate the origin of oxidation in the synthesized 1T-CrTe$_2$ layers. The dissociative adsorption of O$_2$, a critical step in oxidization-related material degradation, is exothermic, releasing a piece of energy of 0.06 eV per O atom on the 1T-CrTe$_2$ surface. This differs from the endothermic adsorption observed on the CrSe$_2$ surface,[38] suggesting that the subsequent oxidation reactions will occur spontaneously at finite temperatures. Given the high oxidation ratio of ≈10%, predominantly observed on the 1T-CrTe$_2$ surface in our

experiments (Figures 1e and 2e), we further investigate the extent of oxidation in the top two surface layers of the few-layer 1T-CrTe$_2$. For simplicity, we focus on a 6L 1T-CrTe$_2$ model, the thinnest 1T-CrTe$_2$ film available in our experiments. The formation enthalpies of various oxidization configurations of 6L 1T-CrTe$_2$ are presented in **Figures 5a** and S8 (Supporting Information). Among all configurations considered, the O$_{Te}$ substitutional impurity (CrTe$_{2-x}$O$_x$) is the most energetically favorable. Our calculations indicate that the O$_{Te}$ substitutional impurity is prone to occur in the surface layers rather than the bulk layers, consistent with our AES results that predominately detected O KLL signals from the surface layers. Substituted Te atoms have a tendency to intercalate at the vdW gap (CrTe$_{2-x}$O$_x$Te$_x$), with a negative formation entropy of −1.75 eV.

Incorporating the O$_{Te}$ substitutional impurity and/or the Te intercalation offers a potential route to modulate the magnetic properties of 1T-CrTe$_2$. The interlayer magnetic coupling of 1T-CrTe$_2$ is dominated by the competition among Pauli repulsion, Coulomb repulsion, and kinetic energy in vdW gaps.[38,39] In a multilayered 1T-CrTe$_2$ system, the surface layer is attracted by dispersion forces in only one direction, resulting in a 0.2 Å shortened interlayer distance between the top two surface layers. The 0.2 Å reduction in the interlayer distance between the two upper surface layers enhances the Pauli repulsion, favoring interlayer
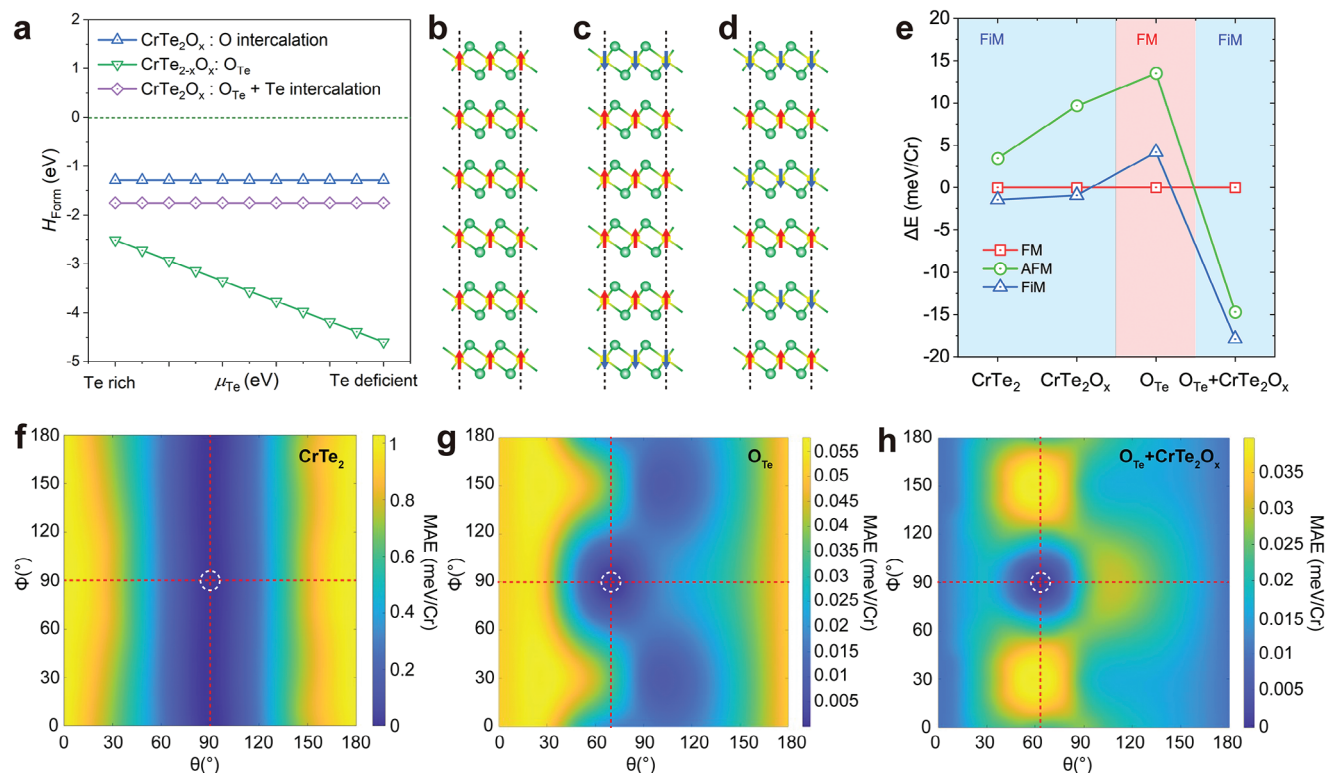
**ADVANCED
SCIENCE NEWS**

www.advancedsciencenews.com

**ADVANCED
MATERIALS**

www.advmat.de

Figure 5. Oxidation influence on magnetism of few-layer 1T-CrTe$_2$. a) Enthalpies of formation for the O intercalations, antisite defects O$_{Te}$, and Te intercalations resulting from Te atoms escaping from O-occupied Te sites. b–d) Schematic representations of interlayer magnetic orders, including (b) FM, (c) FiM, and (d) AFM are depicted. e) Relative total energies of the FM (red rectangles), FiM (blue triangles), and interlayer AFM (green circles) orders of 6L 1T-CrTe$_2$ with different types of oxidation defects. The reference zero is chosen as the energies of the FM order. f–h) Angular dependence of the calculated MAE of 6L 1T-CrTe$_2$ (f) and 1T-CrTe$_2$ with different types of oxidation defects. Here, θ and ϕ correspond to the angles between the magnetization direction and the z and x axes, respectively. A step size of 10° was used in our calculations. The total energy of the Cr moment oriented to the easy axis direction was chosen as the zero-energy reference.

antiferromagnetic coupling between the surface layers[39] and causing ferrimagnetism (FiM). As shown in Figure 5c, the FiM state remains the magnetic ground state even with O substitution or Te intercalation (corresponding to CrTe$_{2-x}$O$_x$ and CrTe$_{2-x}$O$_x$Te$_x$). However, in the presence of only O$_{Te}$ substitutional impurity without Te intercalations, the FM order (Figure 5b) becomes the magnetic ground state. Figure 5e reveals that the values of relative energies between the FM and interlayer AFM or FiM orders increase by at least twofold following oxidation, indicating a substantial enhancement in interlayer spin exchange coupling. Moreover, the antiferromagnetic coupled magnetic moments of the surface and bulk layers do not flip synchronously in a magnetic field, resulting in the appearance of a step-like feature observed in our M-H curves.

Additionally, the oxidation-introduced O$_{Te}$ substitutional impurity and/or Te intercalation can profoundly change the electronic state occupation near the Fermi level, thereby modifying the magnetic anisotropic energies and the direction of the magnetic easy axis.[40–42] As shown in Figure 5f, in pristine 6L 1T-CrTe$_2$, the magnetic moments predominately align along the y direction, consistent with the bulk CrTe$_2$ behavior. However, O substitution in 1T-CrTe$_2$, either without (CrTe$_{2-x}$O$_x$) or with Te intercalation (CrTe$_{2-x}$O$_x$Te$_x$), causes the magnetic moment to tilt ≈70° or 60° off the z-axis (Figure 5g,h). These tilted magnetic

moments result in a spin-flop transition under small critical magnetic fields, giving rise to a noncollinear spin texture in 1T-CrTe$_2$.[43] Since the oxidation preferentially occurs at the surface, the high concentration of O substitution could prevent further oxidation from O atoms penetrating deeper into the bulk layers, allowing the intrinsic magnetic characteristics of 1T-CrTe$_2$ in thicker layers to prevail. Consequently, the easy axis direction in thicker samples is prone to orient in the in-plane y direction.[20]

3. Conclusion

In summary, we have demonstrated the synthesis of wafer-scale uniform 1T-CrTe$_2$ films in a cost-effective PECVD method, which significantly reduces synthesis temperature to less than 400 °C, compatible with the fabrication of BEOL (back-end-of-the-line) devices of Si-COMS technologies. We have found that Te and O coexisted to form CrO$_x$Te$_y$ at the initial reaction stage, which finally transformed into 1T-CrTe$_2$. The 1T-CrTe$_2$ films exhibit perpendicular magnetic anisotropy and special step-like magnetic transition features. Our DFT calculations have shown that the surface oxidation in 1T-CrTe$_2$ films has a great influence on magnetic anisotropy and the special FiM magnetic ground state may be the origin of the observed step-like characters. This unique

magnetic order as observed on our wafer-scale 1T-CrTe$_2$ films provides opportunities to understand the magnetic properties of 2D magnetic materials and apply for novel spintronic devices. Also, our study suggests that it is necessary to further explore approaches to mitigate degradation of the intrinsic magnetic properties or modify the magnetic properties of the materials so that these materials are more in line with the actual application scenarios.

4. Experimental Section

PECVD Synthesis of 1T-CrTe$_2$: A Cr seed layer of 0.6–3.0 nm was deposited on a 2-inch SiO$_2$ (300 nm)/Si substrate by magnetron sputtering regarded as the Cr source, and tellurium (Te, 99.999%, SCR) powder was used as the Te source. To remove impurities from the PECVD system, the process chamber was purged with Ar for 3 times following gas cleaning with 100 sccm Ar for 10 min after loading Cr/SiO$_2$/Si substrate. Next, the process chamber was warmed up to 110 °C and hold for 10 min to further remove residual H$_2$O. Then, the substrate was heated to the designed temperature, saying 370 °C, within 15 min under an Ar atmosphere. After that, 25 sccm H$_2$ and 15 sccm Ar were introduced into the chamber, and plasma was generated at various powers for 120 min to tellurize the Cr seed layer completely. After the reaction, the chamber was quickly cooled to room temperature under an Ar atmosphere.

Sample Characterizations: The Raman spectra were performed using a Renishaw InVia system under 532 nm laser excitation at room temperature. Powder XRD experiments were performed by the Shimadzu XRD-700 diffractometer using Cu Kα radiation ($\lambda = 0.15418$ nm) at room temperature with a voltage of 40 kV and a current of 40 mA. The AES measurements were carried out with a scanning Auger electron spectroscope ULVAC-PHI 710, and the voltage of the primary electron beam was 5 kV. Please note that AES may cause irradiation damage to samples which depends on electron beam energy and exposure dose.[28,44] Empirically, the primary electron beam energy should be $\approx$10 times to the measured Auger electron energy. Consequently, all the AES spectra of the samples were acquired with a primary electron beam of 5 kV to minimize the irradiation damage and ensure the accuracy of the data. The equipped Ar ion gun with a voltage of 1 kV was used for depth profile in the scanning Auger electron spectroscope. The AES Profile technique operated as follows: Ar ion with the voltage of 1 kV was used to etch CrTe$_2$ samples first, and every single etching time was set to 0.2 min. Then AES multiplex spectrum was collected, and the Te/Cr atomic ratio was calculated after each collection. The XPS measurement was performed by ThermoFisher SCIENTIFIC ESCALAB Xi+ equipped with a monochromatic Al Kα X-ray source (hν = 1486.6 eV). The sample's morphology was observed by a spherical aberration-corrected transmission microscope (Tian G2 60–300, FEI). Quantum Design MPMS3 obtained temperature-dependent magnetization hysteresis loops. The PECVD-synthesized CrTe$_2$ sample was preserved in N$_2$ gas during transportation and tested in the MPMS system as quickly as possible to avoid possible degradation. The MBE-RHEED system was used for RHEED measurement. RHEED measurement was conducted using a 14 keV electron gun after baking pretreatment. The electrical transport measurements of the Hall bar device were performed in a Quantum Design physical properties measurement system (PPMS) in a Hall bar configuration with lateral dimensions of 100 µm × 500 µm.

Computational Methods: The calculations were performed using the generalized gradient approximation and projector augmented-wave method[45] as implemented in the Vienna *ab-initio* simulation package.[46] A uniform Monkhorst–Pack k mesh of 21 × 21 × 1 was adopted for integration over the Brillouin zone. A kinetic energy cutoff of 700 eV and 600 eV for the plane-wave basis set was used for the structural relaxation and electronic structure calculations, respectively. A sufficiently large vacuum layer over 20 Å along the out-of-plane direction was adopted to eliminate the interaction among layers. Dispersion correction was performed at the vdW-DF level,[47] with the optB86b functional for the exchange

potential,[48] which was proven to be accurate in describing the structural properties of layered materials.[39,43,49] and was adopted for structural-related calculations in this study. The lattice of pristine few-layer 1T-CrTe$_2$ was adopted and kept fixed during the structure relaxation process. All atoms were allowed to relax until the residual force per atom was less than 0.01 eV Å^{-1} in the calculations when considering different oxidation configurations. To compare energy among different magnetic configurations, the PBE functional.[50] was used based on the vdW-DF-optimised atomic structures. The on-site Coulomb interaction to the Cr d orbitals had U and J values of 2.0 and 0.6 eV, respectively, as revealed by a linear response method[51] and comparison with the results of HSE06.[52] These values were comparable to those adopted in modeling CrI$_3$,[4] CrS$_2$,[53] and CrSe$_2$.[38,39] The role of U values on the predicted magnetic ground state and the logic of choosing a proper U value are discussed elsewhere. The magnetic easy axis was identified using the Renmin Magnetic Easy Axis Finder (ReMEAF) toolkit,[54] which utilizes the simulated annealing algorithm and invokes VASP to determine the global easy-axis orientation. MAEs were calculated for certain angles and used linear interpolation to generate the continuous plots. Formation enthalpies of CrTe$_2$ with different types of oxidation defect configurations are calculated using the total energy method defined as Equation (1):

$$\Delta H_{Form} = E_{CrTe2+O} - E_{CrTe2} - m \times \mu_{Te} - n \times \mu_O \tag{1}$$

where μ_{Te} and μ_O are the chemical potential of the added Te and O atoms to form the oxidated CrTe$_2$. The formation enthalpy (H$_{Form}$) of the CrTe$_2$ with oxidation is plotted as a function of Te chemical potential in Figure 5a. The value of x in CrTe$_2$Ox was set to 0.16 in the calculations, corresponding to an oxidation rate of $\approx$16%. This is consistent with the experimental observed over 10% oxygen content in the sample. Oxidation was confined to the top two layers of the 1T-CrTe$_2$ films in the calculations results shown in Figure 5. This assumption aligns with calculated the formation energies (Figure S8, Supporting Information) and experimental findings, where oxidation was most pronounced at the surface. Oxidation concentration, oxidation distribution, and number of layers used in the calculation models do not qualitatively change our conclusions (Figures S9, S10, Supporting Information).

Supporting Information

Supporting Information is available from the Wiley Online Library or from the author.

Conflict of Interest

The authors declare no conflict of interest.

**ADVANCED
SCIENCE NEWS**

www.advancedsciencenews.com

**ADVANCED
MATERIALS**

www.advmat.de

Data Availability Statement

The data that support the findings of this study are available from the corresponding author upon reasonable request.

[1] B. Huang, G. Clark, E. Navarro-Moratalla, D. R. Klein, R. Cheng, K. L. Seyler, D. Zhong, E. Schmidgall, M. A. McGuire, D. H. Cobden, W. Yao, D. Xiao, P. Jarillo-Herrero, X. Xu, *Nature* **2017**, *546*, 270.

[2] C. Gong, L. Li, Z. Li, H. Ji, A. Stern, Y. Xia, T. Cao, W. Bao, C. Wang, Y. Wang, Z. Q. Qiu, R. J. Cava, S. G. Louie, J. Xia, X. Zhang, *Nature* **2017**, *546*, 265.

[3] H. Wagner, N. D. Mermin, *Phys. Rev. Lett.* **1966**, *17*, 1133.

[4] C. Wang, D. Chen, Z. Zhong, Z. Yuan, Z. Lu, W. Ji, P. Jiang, *Phys. Rev. B* **2019**, *99*, 144401.

[5] Z. Sun, Y. Yi, T. Song, G. Clark, B. Huang, Y. Shan, S. Wu, D. Huang, C. Gao, Z. Chen, M. McGuire, T. Cao, D. Xiao, W. Liu, W. Yao, X. Xu, S. Wu, *Nature* **2019**, *572*, 497.

[6] M. Janoschek, D. S. Chaves, J. C. Cezar, T. Durakiewicz, F. Ronning, Y. Sassa, M. Mansson, B. L. Scott, N. Wakeham, E. D. Bauer, J. D. Thompson, J. Zhu, *Phys. Rev. B* **2016**, *93*, 144404.

[7] Z. Fei, B. Huang, P. Malinowski, W. Wang, T. Song, J. Sanchez, W. Yao, D. Xiao, X. Zhu, A. F. May, W. Wu, D. H. Cobden, J. Chu, X. Xu, *Nat. Mater.* **2018**, *17*, 778.

[8] Y. Wu, Y. Hu, C. Wang, X. Zhou, X. Hou, W. Xia, Y. Zhang, J. Wang, Y. Ding, J. He, P. Dong, S. Bao, J. Wen, Y. Guo, K. Watanabe, T. Taniguchi, W. Ji, Z. Wang, J. Li, *Adv. Mater.* **2023**, *35*, 2302568.

[9] M. R. Habib, S. Wang, W. Wang, H. Xiao, S. M. Obaidulla, A. Gayen, Y. Khan, H. Chen, M. Xu, *Nanoscale* **2019**, *11*, 20123.

[10] H. Xiao, W. Zhuang, L. Loh, T. Liang, A. Gayen, P. Ye, M. Bosman, G. Eda, X. Wang, M. Xu, *Adv. Mater. Interfaces* **2022**, *9*, 2201353.

[11] Y. Zhang, J. Chu, L. Yin, T. A. Shifa, Z. Cheng, R. Cheng, F. Wang, Y. Wen, X. Zhan, Z. Wang, J. He, *Adv. Mater.* **2019**, *31*, 1900056.

[12] M. Huang, S. Wang, Z. Wang, P. Liu, J. Xiang, C. Feng, X. Wang, Z. Zhang, Z. Wen, H. Xu, G. Yu, Y. Lu, W. Zhao, S. A. Yang, D. Hou, B. Xiang, *ACS Nano* **2021**, *15*, 9759.

[13] X. Sun, W. Li, X. Wang, Q. Sui, T. Zhang, Z. Wang, L. Liu, D. Li, S. Feng, S. Zhong, H. Wang, V. Bouchiat, M. Nunez Regueiro, N. Rougemaille, J. Coraux, A. Purbawati, A. Hadj-Azzem, Z. Wang, B. Dong, X. Wu, T. Yang, G. Yu, B. Wang, Z. Han, X. Han, Z. Zhang, *Nano Res.* **2020**, *13*, 3358.

[14] R. Chua, J. Zhou, X. Yu, W. Yu, J. Gou, R. Zhu, L. Zhang, M. Liu, M. B. H. Breese, W. Chen, K. P. Loh, Y. P. Feng, M. Yang, Y. L. Huang, A. T. S. Wee, *Adv. Mater.* **2021**, *33*, 2103360.

[15] J. Liu, B. Ding, J. Liang, X. Li, Y. Yao, W. Wang, *ACS Nano* **2022**, *16*, 13911.

[16] H. Wang, Y. Wen, X. Zhao, R. Cheng, L. Yin, B. Zhai, J. Jiang, Z. Li, C. Liu, F. Wu, J. He, *Adv. Mater.* **2023**, *35*, 2211388.

[17] Z. Li, W. Xia, H. Su, Z. Yu, Y. Fu, L. Chen, X. Wang, N. Yu, Z. Zou, Y. Guo, *Sci. Rep.* **2020**, *10*, 15345.

[18] G. Zhang, F. Guo, H. Wu, X. Wen, L. Yang, W. Jin, W. Zhang, H. Chang, *Nat. Commun.* **2022**, *13*, 5067.

[19] D. C. Freitas, R. Weht, A. Sulpice, G. Remenyi, P. Strobel, F. Gay, J. Marcus, M. Núñez-Regueiro, *J. Phys.: Condens. Matter* **2015**, *27*, 176002.

[20] L. Meng, Z. Zhou, M. Xu, S. Yang, K. Si, L. Liu, X. Wang, H. Jiang, B. Li, P. Qin, P. Zhang, J. Wang, Z. Liu, P. Tang, Y. Ye, W. Zhou, L. Bao, H. Gao, Y. Gong, *Nat. Commun.* **2021**, *12*, 809.

[21] X. Zhang, Q. Lu, W. Liu, W. Niu, J. Sun, J. Cook, M. Vaninger, P. F. Miceli, D. J. Singh, S. Lian, T. Chang, X. He, J. Du, L. He, R. Zhang, G. Bian, Y. Xu, *Nat. Commun.* **2021**, *12*, 2492.

[22] X. Zhang, Y. Li, Q. Lu, X. Xiang, X. Sun, C. Tang, M. Mahdi, C. Conner, J. Cook, Y. Xiong, J. Inman, W. Jin, C. Liu, P. Cai, E. J. G. Santos, C. Phatak, W. Zhang, N. Gao, W. Niu, G. Bian, P. Li, D. Yu, S. Long, *Adv. Mater.* **2024**, *36*, 2311591.

[23] S. Kwon, G. J. de Coster, R. K. Lake, M. R. Neupane, Y. Liu, *Phys. Rev. Mater.* **2022**, *6*, 84004.

[24] C. Ahn, J. Lee, H. Kim, H. Bark, M. Jeon, G. H. Ryu, Z. Lee, G. Y. Yeom, K. Kim, J. Jung, Y. Kim, C. Lee, T. Kim, *Adv. Mater.* **2015**, *27*, 5223.

[25] J. C. Slater, *J. Chem. Phys.* **1964**, *41*, 3199.

[26] A. Purbawati, J. Coraux, J. Vogel, A. Hadj-Azzem, N. Wu, N. Bendiab, D. Jegouso, J. Renard, L. Marty, V. Bouchiat, A. Sulpice, L. Aballe, M. Foerster, F. Genuzio, A. Locatelli, T. O. Menteş, Z. V. Han, X. Sun, M. Núñez-Regueiro, N. Rougemaille, *ACS Appl. Mater. Interfaces* **2020**, *12*, 30702.

[27] Y. Ou, W. Yanez, R. Xiao, M. Stanley, S. Ghosh, B. Zheng, W. Jiang, Y. Huang, T. Pillsbury, A. Richardella, C. Liu, T. Low, V. H. Crespi, K. A. Mkhoyan, N. Samarth, *Nat. Commun.* **2022**, *13*, 2972.

[28] M. Xu, D. Fujita, J. Gao, N. Hanagata, *ACS Nano* **2010**, *4*, 2937.

[29] T. Liang, G. He, G. Huang, Y. Kong, W. Fu, H. Chen, Q. Wang, H. Iwai, D. Fujita, Y. Liu, M. Xu, *Adv. Mater.* **2015**, *27*, 6404.

[30] H. Kim, D. Kim, S. Jung, M. Bae, Y. J. Yun, S. N. Yi, J. Yu, J. Kim, D. H. Ha, *J. Raman Spectrosc.* **2018**, *49*, 1938.

[31] F. Liang, H. Xu, X. Wu, C. Wang, C. Luo, J. Zhang, *Chin. Phys. B* **2018**, *27*, 037802.

[32] P. Colomban, A. Slodczyk, *Opt. Mater.* **2009**, *31*, 1759.

[33] T. Liang, S. Xie, Z. Huang, W. Fu, Y. Cai, X. Yang, H. Chen, X. Ma, H. Iwai, D. Fujita, N. Hanagata, M. Xu, *Adv. Mater. Interfaces* **2017**, *4*, 1600687.

[34] C. Tan, J. Lee, S. Jung, T. Park, S. Albarakati, J. Partridge, M. R. Field, D. G. McCulloch, L. Wang, C. Lee, *Nat. Commun.* **2018**, *9*, 1554.

[35] Z. Chen, Y. Yang, T. Ying, J. Guo, *Nano Lett.* **2024**, *24*, 993.

[36] C. R. Buechler, L. B. Sorensen, J. J. Turner, S. D. Kevan, E. A. Jagla, J. M. Deutsch, T. Mai, O. Narayan, J. E. Davies, K. Liu, J. H. Dunn, K. M. Chesnel, J. B. Kortright, O. Hellwig, E. E. Fullerton, M. S. Pierce, *Phys. Rev. Lett.* **2005**, *94*, 17202.

[37] M. Lohmann, T. Su, B. Niu, Y. Hou, M. Alghamdi, M. Aldosary, W. Xing, J. Zhong, S. Jia, W. Han, R. Wu, Y. Cui, J. Shi, *Nano Lett.* **2019**, *19*, 2397.

[38] B. Li, Z. Wan, C. Wang, P. Chen, B. Huang, X. Cheng, Q. Qian, J. Li, Z. Zhang, G. Sun, B. Zhao, H. Ma, R. Wu, Z. Wei, Y. Liu, L. Liao, Y. Ye, Y. Huang, X. Xu, X. Duan, W. Ji, X. Duan, *Nat. Mater.* **2021**, *20*, 818.

[39] X. Zhou, L. Zhou, Y. Pan, Z. Lu, X. Wan, X. Wang, W. Ji, C. Wang, *Phys. Rev. B* **2020**, *102*, 20402.

[40] R. Wu, J. Hu, *Phys. Rev. Lett.* **2013**, *110*, 97202.

[41] R. Wu, A. J. Freeman, D. Wang, *Phys. Rev. B* **1993**, *47*, 14932.

[42] Z. Zhang, C. Wang, P. Guo, L. Zhou, Y. Pan, Z. Hu, W. Ji, *Phys. Rev. B* **2025**, *111*, 054422.

[43] J. Xian, C. Wang, J. Nie, R. Li, M. Han, J. Lin, W. Zhang, Z. Liu, Z. Zhang, M. Miao, Y. Yi, S. Wu, X. Chen, J. Han, Z. Xia, W. Ji, Y. Fu, *Nat. Commun.* **2022**, *13*, 257.

[44] M. Xu, D. Fujita, N. Hanagata, *Nanotechnology* **2010**, *21*, 265705.

[45] P. E. Blöchl, *Phys. Rev. B* **1994**, *50*, 17953.

[46] J. Furthmüller, G. Kresse, *Phys. Rev. B* **1996**, *54*, 11169.

[47] H. Rydberg, E. Schröder, D. C. Langreth, B. I. Lundqvist, M. Dion, *Phys. Rev. Lett.* **2004**, *92*, 246401.

[48] D. R. Bowler, A. Michaelides, J. Klimeš, *Phys. Rev. B* **2011**, *83*, 195131.

[49] J. Qiao, Y. Pan, F. Yang, C. Wang, Y. Chai, W. Ji, *Sci. Bull.* **2018**, *63*, 159.

[50] K. Burke, M. Ernzerhof, J. P. Perdew, *Phys. Rev. Lett.* **1996**, *77*, 3865.

[51] S. de Gironcoli, M. Cococcioni, *Phys. Rev. B* **2005**, *71*, 35105.

[52] J. Heyd, G. E. Scuseria, M. Ernzerhof, *J. Chem. Phys.* **2003**, *118*, 8207.

[53] X. Zhou, Y. Pan, J. Qiao, X. Kong, C. Kaun, W. Ji, C. Wang, *Phys. Rev. B* **2018**, *97*, 245409.

[54] C. Wang, W. Ji, Renmin Magnetic Easy Axis Finder (ReMEAF) toolkit, https://gitee.com/jigroupruc/re-meaf (accessed: January 2023).